

# Defect-Induced Band Gap Narrowed CeO<sub>2</sub> Nanostructures for Visible Light Activities

Mohammad Mansoob Khan,<sup>†</sup> Sajid Ali Ansari,<sup>†</sup> Debabrata Pradhan,<sup>‡</sup> Do Hung Han,<sup>†</sup> Jintae Lee,<sup>†</sup> and Moo Hwan Cho<sup>\*†</sup>

<sup>†</sup>School of Chemical Engineering, Yeungnam University, Gyeongsan-si, Gyeongbuk 712-749, South Korea

<sup>‡</sup>Materials Science Centre, Indian Institute of Technology, Kharagpur, W. B. 721302, India

## S Supporting Information

**ABSTRACT:** This work reports an electron beam irradiation (30 kGy and 90 kGy) approach to narrow the band gap of the pristine CeO<sub>2</sub> nanostructure (p-CeO<sub>2</sub>) to enhance their visible light activity through defect engineering. This was confirmed by diffuse reflectance spectroscopy, photoluminescence, Raman spectroscopy, X-ray diffraction, X-ray photoelectron spectroscopy (XPS), Brunauer–Emmett–Teller, electrochemical impedance spectroscopy, and linear scan voltammetry. XPS revealed changes in the surface states, composition, Ce<sup>4+</sup> to Ce<sup>3+</sup> ratio, and other defects in the modified CeO<sub>2</sub> nanostructures (m-CeO<sub>2</sub>). The m-CeO<sub>2</sub> exhibits excellent photocatalytic activities by degrading 4-nitrophenol and methylene blue in the presence of visible light ( $\lambda > 400$  nm) compared to the p-CeO<sub>2</sub>. The optical, photocatalytic, and photoelectrochemical studies and proposed mechanism further support the enhanced visible light photocatalytic activities of the m-CeO<sub>2</sub>. This study confirmed that defect-induced band gap engineered m-CeO<sub>2</sub> could be used effectively as photocatalyst and photoelectrodes owing to their enhanced visible light photocatalytic activities.

## INTRODUCTION

The chemistry that occurs at the surfaces of metal oxides has attracted considerable attention for a range of industrial applications including catalysis, photocatalysis, optical display technology, solar energy devices, corrosion prevention, and three-way automotive catalytic converters.<sup>1–3</sup> Among the metal oxides, CeO<sub>2</sub> is an important rare earth oxide that has attracted considerable attention for use in catalysis, fuel cells, UV-blockers, sensors, oxygen storage capacitors, and biological applications.<sup>1–5</sup> CeO<sub>2</sub> is a wide band gap semiconductor (~3.4 eV), which limits its use as an electronic material for logic operations and photocatalyst.<sup>1–4</sup> The chemical functionalization of CeO<sub>2</sub> is a well-known method for tuning the band structure and majority carrier type for electronic and optical applications.<sup>1–3,6</sup> Nevertheless, few studies have reported the extent to which the band gap can be tuned electrochemically. On the other hand, there are several reports on tuning the band gap energy of metal oxides by doping with nonmetals and metals.<sup>7–10</sup>

Few studies showed that the electron beam (EB) can be used for the synthesis of different metal nanoparticles and thin films of metal oxides with the desired properties.<sup>11–16</sup> This approach has several advantages over other methods, such as scalability and an ability to interact effectively with all types of materials (including high band gap semiconductors, oxides, etc.) through coulomb interactions created by charged particles, i.e. electrons.<sup>11–16</sup> Recently, it was reported that, as an alternative, chemical doping can be achieved by ionizing irradiation, such as EB or  $\gamma$  radiation.<sup>17,18</sup> Radiation-induced nanoparticles and supported catalysts exhibit particularly high efficiency and selectivity in catalysis due to their small size, monodisperse, and probably their strong adhesion to the support.<sup>18</sup> Recent reports showed that an EB can be used to create defects in

materials.<sup>13–19</sup> Defects, such as oxygen vacancies and step edges, are the most reactive sites on the surface of metal oxides.<sup>13,15,19,20</sup> Industrially, CeO<sub>2</sub> is one of the most interesting oxides because oxygen vacancy defects can be formed and eliminated rapidly, giving them high “oxygen storage capacity”.<sup>1,3</sup> Control of the density and nature of oxygen vacancies can provide a means of tailoring the reactivity of ceria-based catalysts.<sup>1–3</sup>

Synthesizing CeO<sub>2</sub> with low band gap energy is a challenge. Recently, we used EB to substantially decrease the band gap of TiO<sub>2</sub> by creating different type of defects.<sup>19</sup> Therefore, this approach was further extended to tune the wide band gap of commercially available CeO<sub>2</sub> to the desired (low) band gap energy without doping with any transition metals or nonmetals. To the best of the author’s knowledge, this is the first report of using EB to decrease the band gap energy of CeO<sub>2</sub> without doping. The modified CeO<sub>2</sub> showed outstanding photo-degradation of 4-nitrophenol (4-NP) and methylene blue (MB) under visible light ( $\lambda > 400$  nm) irradiation. Electrochemical impedance spectroscopy (EIS) and linear scan voltammetry (LSV) studies in the dark and under visible light irradiation confirmed the substantial decrease in charge transfer resistance and minimizing the recombination of photo-generated electrons and holes, whereas LSV further confirms the enhancement in the photocurrent of the modified CeO<sub>2</sub> (30 kGy and 90 kGy) nanostructures, which support their enhanced photocatalytic activities, and potential use as a photocatalyst and photoelectrode. Hereafter, pure CeO<sub>2</sub> and

**Received:** March 7, 2014

**Revised:** May 15, 2014

**Accepted:** May 19, 2014

**Published:** May 19, 2014

modified CeO<sub>2</sub> (30 kGy and 90 kGy) are abbreviated as p-CeO<sub>2</sub>, 30 kGy-CeO<sub>2</sub>, and 90 kGy-CeO<sub>2</sub>, respectively.

## EXPERIMENTAL SECTION

**Materials.** The CeO<sub>2</sub> nanostructure and MB were purchased from Sigma-Aldrich, whereas sodium acetate, *p*-nitrophenol (4-NP), and sodium sulfate (Na<sub>2</sub>SO<sub>4</sub>) were obtained from Duksan Pure Chemicals Co. Ltd. South Korea and were used as received. Ethyl cellulose and  $\alpha$ -terpineol were purchased from KANTO Chemical Co., Japan. Fluorine doped transparent conducting oxide glass (FTO; F-doped SnO<sub>2</sub> glass; 7  $\Omega$ /sq) was obtained from Pilkington, U.S.A. All other chemicals used in this study were of analytical grade and used as received. All solutions were prepared from deionized water obtained using a PURE ROUP 30 water purification system.

**Methods.** An EB accelerator (ELV-0.5, BINP, Russia) with a maximum beam power, maximum beam current, and maximum beam energy of 28 kW, 40 mA, and ~0.7 MeV, respectively, were used to modify p-CeO<sub>2</sub>. The UV-vis diffuse reflectance spectra (DRS) of the powdered samples were obtained using a UV-vis-NIR double beam spectrophotometer (VARIAN, Cary 5000, U.S.A.) equipped with a diffuse reflectance accessory. A He-Cd laser (Kimon, 1 K, Japan) with a wavelength of 325 nm and a power of 50 mW was used as an excitation source for the photoluminescence (PL) measurements at Korea Basic Science Institute (KBSI). X-ray diffraction (XRD, PANalytical, X'pert PRO-MPD, The Netherlands) was performed using Cu K $\alpha$  radiation ( $\lambda = 0.15405$  nm). Raman spectroscopy was performed on HR800 UV Raman microscope (Horiba Jobin-Yvon, France). X-ray photoelectron spectroscopy (XPS, ESCALAB 250 XPS System, Thermo Fisher Scientific U.K.) was conducted with the following X-ray source: monochromated Al K $\alpha$ ,  $h\nu = 1486.6$  eV, X-ray energy: 15 kV, 150 W and spot size: 500  $\mu$ m at KBSI. The XP spectra were fitted using a software "Avantage program". The microstructures of the samples were measured by high resolution transmission electron microscopy (HRTEM, JEM-2100 JEOL) at an operating voltage of 200 kV. Selected-area electron diffraction (SAED) images were recorded by HRTEM. The photocatalytic degradation and photoelectrochemical experiments (for photoelectrodes such as EIS and LSV) were conducted using a 400 W lamp (3M, U.S.A.). The Brunauer-Emmett-Teller (BET) specific surface area of samples was measured using a Belsorp II-mini (BEL, Japan Inc.). The EIS and LSV measurements were carried out using a potentiostat (Versa STAT 3, Princeton Research, U.S.A.) with a standard three-electrode system, in which Ag/AgCl (saturated with KCl), a Pt gauge and Fluorine-doped tin oxide (FTO) glass coated with p-CeO<sub>2</sub>, 30 kGy-CeO<sub>2</sub> or 90 kGy-CeO<sub>2</sub> were used as the reference, counter and working electrodes, respectively, in a 0.2 M Na<sub>2</sub>SO<sub>4</sub> solution as the electrolyte. The working electrodes for EIS and LSV were prepared as follows: 100 mg of each sample was suspended thoroughly by adding ethyl cellulose as the binder and  $\alpha$ -terpineol as the solvent for the paste, and then coated on a FTO glass electrode using a doctor-blade and dried in oven.

**Modification of CeO<sub>2</sub> Nanostructure by Electron Beam.** Commercial CeO<sub>2</sub> nanostructure was modified using an EB accelerator in integral mode with an EB energy of 0.7 MeV and an initial EB current of 2 mA/sec in water at room temperature and atmospheric pressure. Two 75 mL aqueous dispersions of p-CeO<sub>2</sub> (50 mM) were prepared. The initial pH of the aqueous dispersions was 4.40. The final pH of the

aqueous dispersions was 3.93 and 4.08 after exposure to an EB dose of 30 kGy, (power 924 mA.sec and real time 8.8 min) and 90 kGy (power 2724 mA.sec and real time 23.40 min) respectively. The almost white p-CeO<sub>2</sub> changed to a light yellow and pale yellow upon exposure to the 30 and 90 kGy EB dose, respectively. The resulting dispersions were centrifuged and a yellowish powder was obtained in both cases. The 30 kGy-CeO<sub>2</sub> and 90 kGy-CeO<sub>2</sub> nanostructures were dried in an oven at 90 °C, and used for different analyses, photocatalysis, and photoelectrodes.

### Photocatalytic Degradation of 4-NP and MB by p-CeO<sub>2</sub>, 30 kGy-CeO<sub>2</sub> and 90 kGy-CeO<sub>2</sub> Nanostructures.

The photocatalytic activities of the p-CeO<sub>2</sub>, 30 kGy-CeO<sub>2</sub> and 90 kGy-CeO<sub>2</sub> nanostructures were tested for the catalytic degradation of 4-NP (5 mg/L) as well as MB (10 mg/L) and estimated, as reported earlier.<sup>19,20</sup> For the photodecomposition experiment, 2 mg of each photocatalyst was suspended in a 20 mL of the 4-NP and MB aqueous solutions. Each solution was sonicated for 5 min and later stirred in the dark for 30 min to complete the adsorption and desorption equilibrium of the specific substrate on the p-CeO<sub>2</sub>, 30 kGy-CeO<sub>2</sub> and 90 kGy-CeO<sub>2</sub> nanostructures. The solutions were irradiated using a 400 W lamp ( $\lambda > 400$  nm). The two sets of experiments for 4-NP and MB degradation were observed for 5 and 6 h, respectively. The rate of 4-NP and MB degradation was examined by taking 2 mL of the samples from each set every 1 h, centrifuging them to remove the catalyst and recording the UV-vis spectra, from which the degradation of 4-NP and MB was calculated.

As a control experiment, p-CeO<sub>2</sub> nanoparticles (reference photocatalyst, Sigma-Aldrich) were used to degrade 4-NP and MB under same experimental conditions. Each degradation experiment was performed in triplicate to ensure the photocatalytic activity of the p-CeO<sub>2</sub>, 30 kGy-CeO<sub>2</sub>, and 90 kGy-CeO<sub>2</sub> nanostructures. Another blank experiment was performed without any photocatalyst under visible light irradiation for 4-NP and MB under same experimental conditions. The degradation was observed for 5 and 6 h for 4-NP and MB respectively.

The stability and reusability of the 90 kGy-CeO<sub>2</sub> nanostructures was tested after centrifuging the catalyst from 4-NP and MB degraded solutions and tested in a similar manner to that mentioned above. The isolated catalyst from the first and second runs were washed with DI water and dried in an oven at 90 °C and successively reused for the second and third runs to check their catalytic activity with a fresh 4-NP and MB solution under the same conditions.

### Photoelectrochemical Studies of the p-CeO<sub>2</sub>, 30 kGy-CeO<sub>2</sub>, and 90 kGy-CeO<sub>2</sub> Nanostructures.

To examine the photoelectrode response of the p-CeO<sub>2</sub>, 30 kGy-CeO<sub>2</sub>, and 90 kGy-CeO<sub>2</sub> nanostructures, photoelectrochemical experiments, such as EIS and LSV, were conducted under ambient conditions in the dark and under visible light irradiation in a 50 mL, 0.2 M Na<sub>2</sub>SO<sub>4</sub> aqueous solution at room temperature. For each electrode, EIS was first performed in dark conditions and later under visible light irradiation ( $\lambda > 400$  nm) at 0.0 V and with a frequency ranging from 1 to 10<sup>4</sup> Hz. The photocurrent response was obtained by LSV in the dark and under visible light irradiation at a scan rate of 50 mV/s over the potential range, -1.0 to 1.0 V.

## RESULTS AND DISCUSSION

An EB was used as a "defect engineer" because it can create different types of defects in the CeO<sub>2</sub> crystal, thereby imparting

novel characteristics, such as a reduced band gap and visible light photocatalytic activity.<sup>19</sup> This protocol does not involve any expensive and toxic chemicals, which make this modification process quite useful and efficient in the field of nanoparticle modification. The entire process took place in water at room temperature and atmospheric pressure. Figure 1

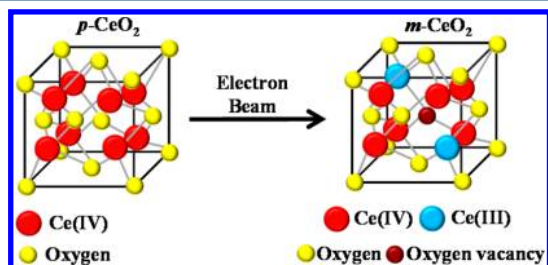


**Figure 1.** Schematic model illustrating the change in crystalline structure of  $\text{CeO}_2$  due to formation of  $\text{Ce(III)}$  and oxygen vacancy after electron beam irradiation.

shows the schematic model illustrating the defect induced band gap narrowing of commercially available  $\text{CeO}_2$  nanostructure by EB, which is simple, easy, fast, and efficient. The high energy electrons generated by EB can either reduce some of the  $\text{Ce}^{4+}$  ions to  $\text{Ce}^{3+}$  or interact with molecules of  $\text{H}_2\text{O}$  as well as air and may form solvated electrons,  $\text{H}^\bullet$ ,  $\text{OH}^\bullet$ , and strong oxidizing agents, such as ozone ( $\text{O}_3$ ) and OH groups. These species may modify the  $\text{CeO}_2$  by forming  $\text{Ce}^{3+}$ , oxygen vacancies, or surface modifications.<sup>11–16,19,21</sup> These  $\text{Ce}^{3+}$ , OH and other species generated in situ modify the commercial  $\text{CeO}_2$  and impart enhanced visible light activities to the 30 kGy- $\text{CeO}_2$  and 90 kGy- $\text{CeO}_2$  nanostructures.

**Optical Properties.** Band gap measurements were carried out by DRS to determine the optical properties of the modified 30 kGy- $\text{CeO}_2$  and 90 kGy- $\text{CeO}_2$  nanostructures that were caused by the EB treatment (Figure 2a). UV–vis DRS of both 30 kGy- $\text{CeO}_2$  and 90 kGy- $\text{CeO}_2$  nanostructures showed the lower reflectance (%R) compared to p- $\text{CeO}_2$  (Figure 2a inset). This suggests that there are some changes in the EB-modified  $\text{CeO}_2$  nanostructures at the molecular level.<sup>6,22</sup> Figure S1 (Supporting Information) presents the UV–vis absorbance of these nanostructures, showing similar trends as well as color of the samples. A desirable band gap is very important for photocatalysis, photoelectrodes and photovoltaic applications.<sup>6</sup> A plot of the Kubelka–Munk function as a function of energy is used to determine the band gap. The two 30 kGy- $\text{CeO}_2$  and 90

kGy- $\text{CeO}_2$  nanostructures samples showed (Figure 2a) different band gaps compared to p- $\text{CeO}_2$ , indicating changes in the optical properties of the 30 kGy- $\text{CeO}_2$  and 90 kGy- $\text{CeO}_2$  nanostructures. The 30 kGy- $\text{CeO}_2$  and 90 kGy- $\text{CeO}_2$  nanostructures showed decrease in band gap energy ( $E_g$ ) from 3.36 eV of p- $\text{CeO}_2$  to 3.15 and 3.12 eV, respectively. This shows that the changes in the %R and band gap of the 30 kGy- $\text{CeO}_2$  and 90 kGy- $\text{CeO}_2$  nanostructures caused by the 30 kGy EB and 90 kGy EB treatments were substantial in comparison to p- $\text{CeO}_2$ . The red-shift in the band gap has been attributed to the presence of  $\text{Ce}^{3+}$  at the grain boundaries, and the band gap decreases with increasing  $\text{Ce}^{3+}$  concentration, which forms some localized gap states in the band gap.<sup>23,24</sup> Tatar et al.<sup>16</sup> reported that the red shift in the band gap is due to the formation of some localized band gap states caused by oxygen vacancies and  $\text{Ce}^{3+}$ . The band gap narrowing of the 30 kGy- $\text{CeO}_2$  and 90 kGy- $\text{CeO}_2$  nanostructures might be due to oxygen vacancies, defects and an increase in  $\text{Ce}^{3+}$ .

**PL Analysis.** PL is closely related to the surface states, oxygen vacancies, defects, and stoichiometry of any semiconductor material. This technique is used to determine the effectiveness of trapping, migration, transfer of charge carriers, as well as for better understanding the fate of the electron–hole pairs in semiconductors.<sup>23,25</sup> In the cubic fluorite structure of  $\text{CeO}_2$ , oxygen ions are not closely packed, and  $\text{CeO}_2$  may form many oxygen vacancies while maintaining the basic fluorite structure.<sup>23</sup> The 30 kGy- $\text{CeO}_2$  and 90 kGy- $\text{CeO}_2$  nanostructures show high PL intensities compared to p- $\text{CeO}_2$  (Figure 2b). This was attributed to the presence of a higher number of oxygen vacancies and/or defects in the 30 kGy- $\text{CeO}_2$  and 90 kGy- $\text{CeO}_2$  nanostructures, which leads to an enhancement of the optical properties.<sup>23,25–27</sup> This observation is in accordance with the UV–vis reflectance spectra (Figure 2a). Liqiang et al. reported that oxygen vacancies and defects can easily bind the photoinduced electrons to form excitons so that the PL signal can occur easily, and the PL signal increases with increasing content of oxygen vacancies or defects.<sup>25,28</sup> Therefore, high intensity PL spectra were observed for the 30 kGy- $\text{CeO}_2$  and 90 kGy- $\text{CeO}_2$  nanostructures compared to p- $\text{CeO}_2$  because of the high content of oxygen vacancies and an increase in  $\text{Ce}^{3+}$  and other defects.<sup>23,25–28</sup> On the other hand, the PL intensity observed in the case of the 90 kGy- $\text{CeO}_2$  nanostructure was higher than that of the 30 kGy- $\text{CeO}_2$  nanostructures, which suggests that in 90 kGy- $\text{CeO}_2$  nanostructures there is a higher separation rate of photoinduced charge carriers, higher

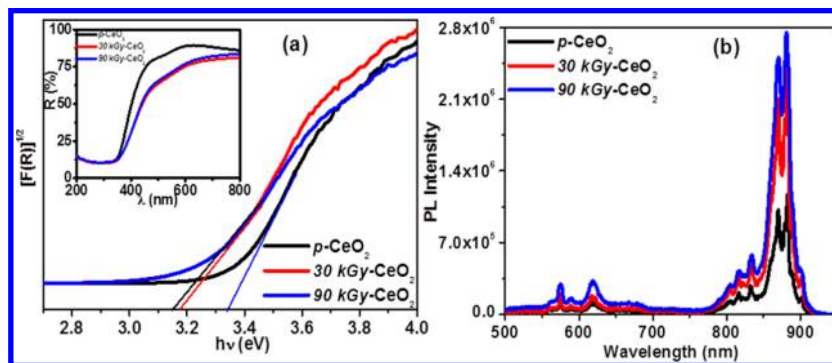


**Figure 2.** (a)  $[F(R)h\nu]^{1/2}$  versus  $h\nu$  plot of the p- $\text{CeO}_2$ , 30 kGy- $\text{CeO}_2$ , and 90 kGy- $\text{CeO}_2$  nanostructures. (Inset) UV–vis diffuse reflectance spectra. (b) PL spectra of the p- $\text{CeO}_2$ , 30 kGy- $\text{CeO}_2$ , and 90 kGy- $\text{CeO}_2$  nanostructures.

separation between the photoelectrons and holes, and higher number of different types of defects.<sup>19,25</sup>

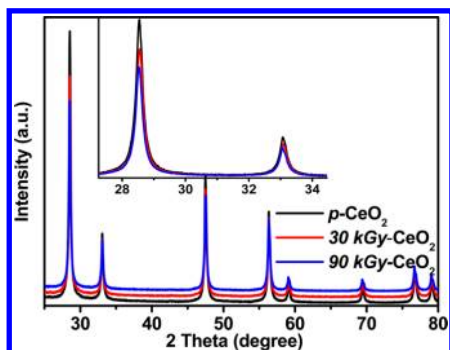


**Figure 3.** XRD patterns of the p-CeO<sub>2</sub>, 30 kGy-CeO<sub>2</sub>, and 90 kGy-CeO<sub>2</sub> nanostructures.

**XRD Analysis.** The phase purity of the modified nanostructures was examined by XRD (Figure 3) to identify the change in the phase and structure of the modified samples. All diffraction peaks from p-CeO<sub>2</sub>, 30 kGy-CeO<sub>2</sub> and 90 kGy-CeO<sub>2</sub> nanostructures could be indexed to the fluorite cubic phase of CeO<sub>2</sub> (JCPDS 81-0792). The peaks at 28.54°, 33.08°, 47.48°, 56.33°, 59.08°, 69.4°, 76.69°, and 79.06° 2θ were assigned to the CeO<sub>2</sub> (111), (200), (220), (311), (222), (400), (331), and (420) planes, respectively. No obvious sign of crystalline Ce<sub>2</sub>O<sub>3</sub> or Ce(OH)<sub>3</sub> were detected. The XRD patterns of the 30 kGy-CeO<sub>2</sub> and 90 kGy-CeO<sub>2</sub> nanostructures were similar to p-CeO<sub>2</sub> except for a minor difference in the peak intensities and peak broadening. This shows that after EB irradiation, the basic structure (fluorite cubic phase) of CeO<sub>2</sub> has not changed, even though the successive decrease in the intensities of 30 kGy-CeO<sub>2</sub> and 90 kGy-CeO<sub>2</sub> indicates a decrease in the crystallinity of the nanostructures. A very small

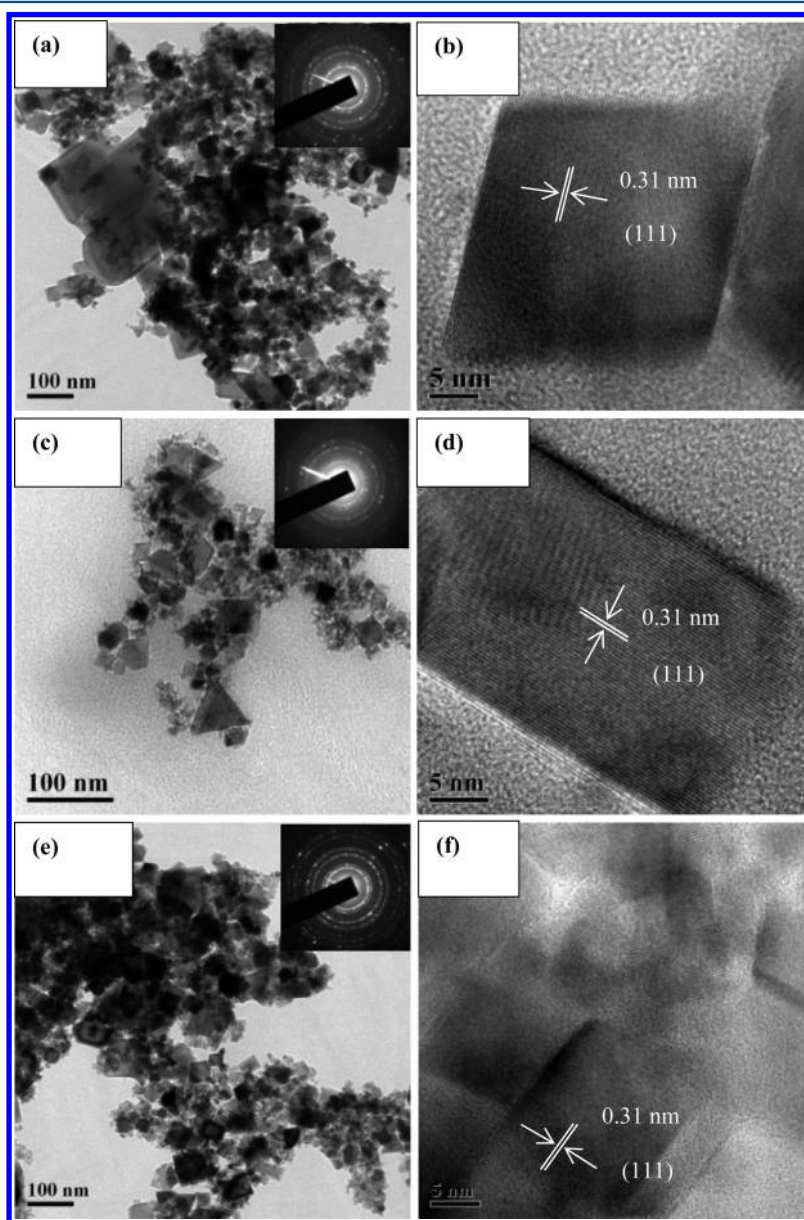


**Figure 4.** TEM and HRTEM images of the (a, b) p-CeO<sub>2</sub>, (c, d) 30 kGy-CeO<sub>2</sub>, and (e, f) 90 kGy-CeO<sub>2</sub>. The insets of (a), (c), and (e) show the SAED pattern of the corresponding sample.

shift of the peaks were observed (Figure 3 inset), which could be due to oxygen vacancies, defects and  $\text{Ce}^{3+}$  that contribute to the development of strain in the XRD pattern, which lead to a change in the particle size.<sup>23</sup> The mean crystallite size of the p-CeO<sub>2</sub>, 30 kGy-CeO<sub>2</sub> and 90 kGy-CeO<sub>2</sub> nanostructures were calculated using the Scherrer's formula,  $D = \kappa\lambda/\beta \cos \theta$ , where  $\kappa$  is the shape factor and has a typical value of approximately 0.9,  $\lambda$  is the wavelength (Cu K $\alpha$  = 0.15405 nm),  $\beta$  is the full width at half-maximum of the most intense peak, and  $\theta$  is the peak position.<sup>29,30</sup> Using this equation, the calculated crystallite size of the p-CeO<sub>2</sub>, 30 kGy-CeO<sub>2</sub> and 90 kGy-CeO<sub>2</sub> nanostructures at  $\sim 28.52^\circ$   $2\theta$  were approximately 22.64 nm, 22.70 and 22.78 nm, respectively (Table 1), which were within the range of the

**Table 1. Structural Parameters Measured from the XRD Patterns of the p-CeO<sub>2</sub>, 30 kGy-CeO<sub>2</sub>, and 90 kGy-CeO<sub>2</sub> Powder**

samples	$2\theta$	$d$ -spacing (Å)	lattice parameters (Å)	volume (Å <sup>3</sup> )
p-CeO <sub>2</sub>	28.52	3.11	$a = b = c = 5.408$	158.22
30 kGy-CeO <sub>2</sub>	28.53	3.12	$a = b = c = 5.409$	158.27
90 kGy-CeO <sub>2</sub>	28.51	3.12	$a = b = c = 5.409$	158.25

particle sizes measured by TEM (Figure 4). After EB irradiation at 30 kGy and 90 kGy, the crystallite size had slightly increased compared to the p-CeO<sub>2</sub> nanostructure (Table 1). A small increase in the crystallite size upon EB irradiation indicates the formation of an amorphous phase and defects at the surface of CeO<sub>2</sub> crystals. This suggests that an EB could be a good tool for modifying the required XRD parameters without changing the basic structure (fluorite cubic phase) for defect induced band gap narrowing of different metal oxides for photocatalysis and photoelectrodes. Similar changes were observed by an EB treatment in the case of TiO<sub>2</sub>.<sup>19,21</sup>

**TEM Analysis.** Figure 4a, c and e shows TEM images of the p-CeO<sub>2</sub>, 30 kGy-CeO<sub>2</sub>, and 90 kGy-CeO<sub>2</sub> samples. The shapes of the CeO<sub>2</sub> particles are nonuniform with a majority observed as cubes. Triangular and diamond shaped particles were also clearly visible in the TEM images. The size of the particles was measured to be in the range of 10 to 100 nm. The ring selected area electron diffraction (SAED) pattern confirmed the polycrystalline nature of the CeO<sub>2</sub> samples (Figure 4 insets). Figure 4b, d and f shows the corresponding HRTEM images with a continuous lattice, indicating the high crystalline nature of CeO<sub>2</sub> nanostructures. A lattice spacing of 0.31 nm, which corresponds to the (111) plane, was measured from the HRTEM images. This is in accordance with the prominent (111) XRD peak. Amorphous regions are also observed (see Figure 4f) around the crystalline particles, suggesting the presence of amorphous Ce<sub>2</sub>O<sub>3</sub> in the samples. The amorphous regions appear to be higher for the 30 kGy-CeO<sub>2</sub> and 90 kGy-CeO<sub>2</sub> nanostructures than p-CeO<sub>2</sub>.

**Raman Analysis.** Figure 5 shows the Raman spectra of p-CeO<sub>2</sub>, 30 kGy-CeO<sub>2</sub>, and 90 kGy-CeO<sub>2</sub> nanostructures at an excitation wavelength of 514 nm. A single and strong peak centered at approximately 465 cm<sup>-1</sup> was observed for the three samples, which was assigned to the F<sub>2g</sub> Raman active symmetrical stretching mode of the CeO<sub>2</sub> cube structure.<sup>6,23,29,31</sup> The Raman spectra of the p-CeO<sub>2</sub>, 30 kGy-CeO<sub>2</sub>, and 90 kGy-CeO<sub>2</sub> nanostructures were similar except for the peak broadening. Peak broadening was observed in the 30 kGy-CeO<sub>2</sub> and 90 kGy-CeO<sub>2</sub> nanostructures compared to the

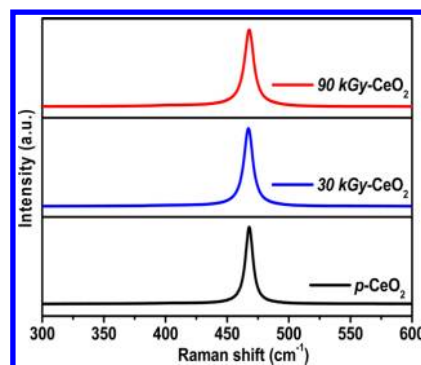


**Figure 5. Raman spectra of the p-CeO<sub>2</sub>, 30 kGy-CeO<sub>2</sub>, and 90 kGy-CeO<sub>2</sub> nanostructures.**

p-CeO<sub>2</sub>, which was attributed to shape alteration, strain, defects in the crystals and  $\text{Ce}^{3+}$  formation.<sup>23,29,31</sup> The peak broadening in the case of 90 kGy-CeO<sub>2</sub> was slightly more than that of the 30 kGy-CeO<sub>2</sub>, which shows a higher concentration of defects,  $\text{Ce}^{3+}$ , and strain in 90 kGy-CeO<sub>2</sub> than 30 kGy-CeO<sub>2</sub>.<sup>23,29,31</sup> These observations are similar to those of DRS, PL and XRD, which further confirms the larger number of defects and strain in the 30 kGy-CeO<sub>2</sub> and 90 kGy-CeO<sub>2</sub> nanostructures compared to p-CeO<sub>2</sub>.<sup>23</sup> Several factors might have affected the changes in the main Raman peak position and line width, including phonon confinement, strain, broadening associated with the size distribution, defects, and variations in phonon relaxation with particle sizes.<sup>31</sup> Oxygen vacancies and  $\text{Ce}^{3+}$  ions in the 30 kGy-CeO<sub>2</sub> and 90 kGy-CeO<sub>2</sub> nanostructures are believed to be responsible for the changes in the Raman spectra, which is further supported by DRS, PL, and XPS.

**XPS Analysis.** The chemical state and composition of the p-CeO<sub>2</sub>, 30 kGy-CeO<sub>2</sub> and 90 kGy-CeO<sub>2</sub> nanostructures were characterized by XPS. Carbon, oxygen and cerium were detected in the XPS survey spectra (Figure S2a, Supporting Information). The C 1s photoelectron peak at 284.5 eV binding energy (BE) was stronger for p-CeO<sub>2</sub> and the intensity of the C 1s feature was reduced for the 30 kGy-CeO<sub>2</sub> and 90 kGy-CeO<sub>2</sub> nanostructures, which was attributed to the removal of surface carbon impurities by EB irradiation (Figure S2b, Supporting Information). Figure 6a, c and e and Figure 6b, d and f show the Ce 3d and O 1s photoelectron peaks of p-CeO<sub>2</sub>, 30 kGy-CeO<sub>2</sub>, and 90 kGy-CeO<sub>2</sub> nanostructures, respectively. The broad Ce 3d photoelectron peaks were deconvoluted to assign precisely and allow an estimation of the composition of different chemical states present in the samples. The major  $\text{Ce}^{4+}$  3d<sub>5/2</sub> ( $\text{Ce}^{4+}$  3d<sub>3/2</sub>) photoelectron peaks for the p-CeO<sub>2</sub>, 30 kGy-CeO<sub>2</sub>, and 90 kGy-CeO<sub>2</sub> nanostructures was observed at a BE of 898.94 eV (916.43 eV), 898.23 eV (916.12 eV), and 898.8 eV (916.32 eV), respectively. Similarly, the main  $\text{Ce}^{3+}$  3d<sub>5/2</sub> ( $\text{Ce}^{3+}$  3d<sub>3/2</sub>) photoelectron peaks for the p-CeO<sub>2</sub>, 30 kGy-CeO<sub>2</sub>, and 90 kGy-CeO<sub>2</sub> nanostructures was observed at a binding energy of 882.96 eV (901.98 eV), 882.03 eV (900.97 eV), and 882.81 eV (901.73 eV), respectively.<sup>32,33</sup> The less intense deconvoluted Ce 3d peaks were assigned to the “shake-up” peaks normally observed in the case of CeO<sub>2</sub>.<sup>32,33</sup> The broad O 1s feature in Figure 6b, d and f was deconvoluted into four oxygen peaks for all the samples. The XPS BE position at 528.37, 530.29, 531.48, and 533.49 eV for the p-CeO<sub>2</sub> sample was assigned to surface adsorbed oxygen, oxygen from CeO<sub>2</sub>, oxygen from Ce<sub>2</sub>O<sub>3</sub>, and Ce(OH)<sub>3</sub> and/or Ce(OH)<sub>4</sub>, respectively.<sup>32</sup> The 30 kGy-CeO<sub>2</sub> and 90 kGy-CeO<sub>2</sub> samples

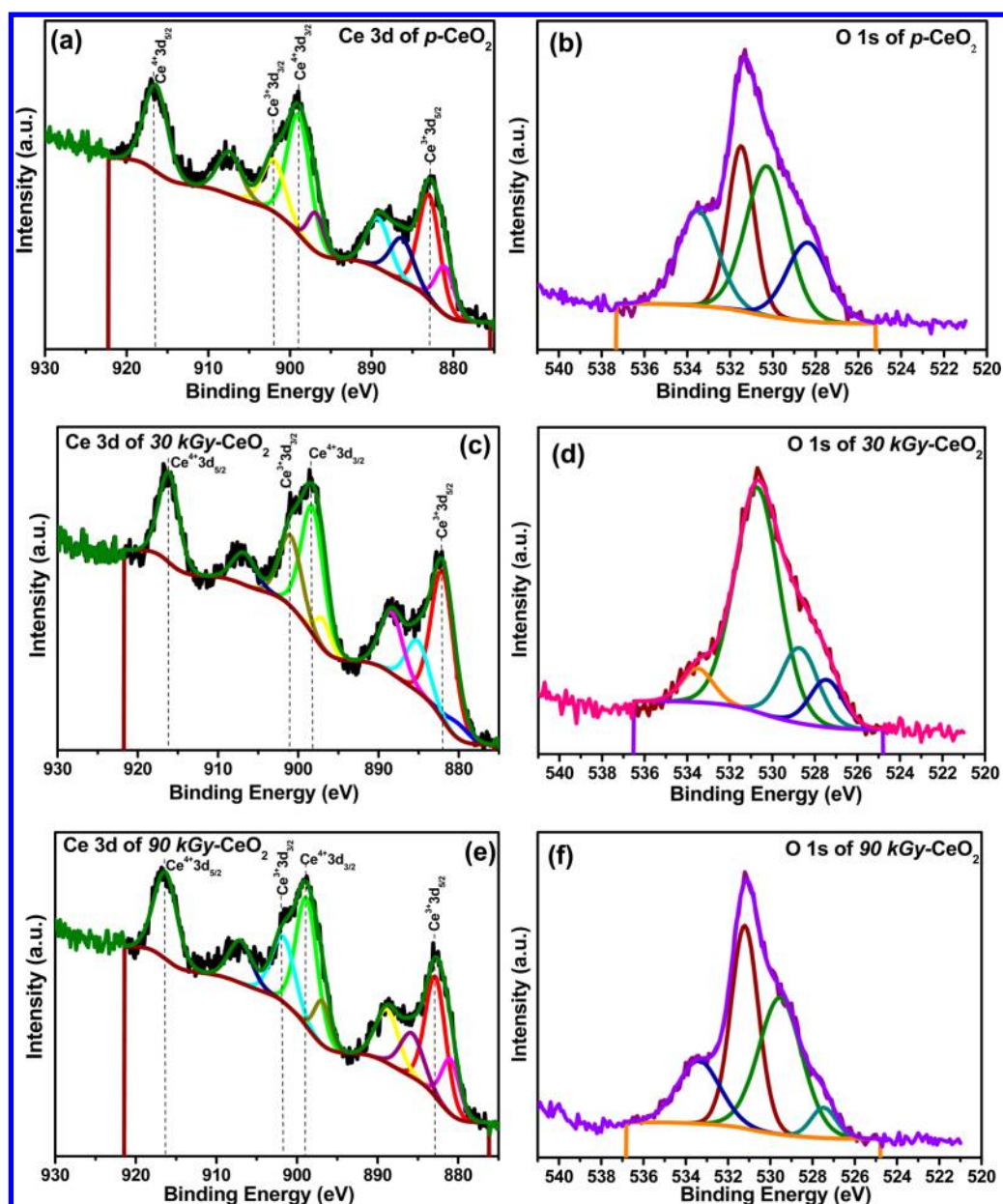


**Figure 6.** Deconvoluted XPS region spectra of Ce 3d (a, c and e) and O 1s (b, d and f) for p-CeO<sub>2</sub> (a and b), 30 kGy-CeO<sub>2</sub> (c and d), and 90 kGy-CeO<sub>2</sub> (e and f).

showed similar O 1s XP spectra. The Ce<sup>3+</sup> to Ce<sup>4+</sup> ratios in the p-CeO<sub>2</sub>, 30 kGy-CeO<sub>2</sub> and 90 kGy-CeO<sub>2</sub> samples were estimated from the deconvoluted peak area (Figure 6a, c, and e).<sup>32</sup> The detailed procedure of the estimation is reported elsewhere.<sup>32</sup> The Ce<sup>3+</sup> concentration increased with increasing the EB irradiation energy. The presence of trivalent Ce<sup>3+</sup> can be due either to the formation of Ce<sub>2</sub>O<sub>3</sub> or oxygen vacancies. To confirm this, the [O]/[Ce] and [O 1s]/[Ce 3d] ratios were measured from their photoelectron peak area considering their sensitivity factor and are tabulated in Table 2.<sup>32,33</sup> The sensitivity factor for Ce and O is 7.399 and 0.711, respectively. Semiquantitative analysis of the integrated peak areas can provide the concentrations of Ce<sup>3+</sup> and Ce<sup>4+</sup> ions in the p-CeO<sub>2</sub>, 30 kGy-CeO<sub>2</sub>, and 90 kGy-CeO<sub>2</sub> nanostructures, as listed in Table 2, using the reported methods and formulas.<sup>32</sup> XPS analysis confirmed the presence of both Ce<sup>4+</sup> and Ce<sup>3+</sup> in all samples and an increase in the Ce<sup>3+</sup> concentration with EB

**Table 2.** Concentrations of Ce<sup>4+</sup> and Ce<sup>3+</sup> Ions and Stoichiometry  $x = [\text{O}]/[\text{Ce}]$  and  $x' = [\text{O 1s}]/[\text{Ce}_{3d}]$  of the p-CeO<sub>2</sub>, 30 kGy-CeO<sub>2</sub>, and 90 kGy-CeO<sub>2</sub> Nanostructures

samples	Ce <sup>4+</sup>	Ce <sup>3+</sup>	$x = [\text{O}]/[\text{Ce}]$	$x' = [\text{O 1s}]/[\text{Ce}_{3d}]$
p-CeO <sub>2</sub>	0.7346	0.2653	1.8671	2.0492
30 kGy-CeO <sub>2</sub>	0.7070	0.2921	1.8622	1.8118
90 kGy-CeO <sub>2</sub>	0.6411	0.3588	1.8205	1.7517

irradiation, which is due to the formation of more defects and/or an amorphous phase of Ce<sub>2</sub>O<sub>3</sub>.

As indicated by XPS and Raman spectroscopy, the 30 kGy-CeO<sub>2</sub> and 90 kGy-CeO<sub>2</sub> nanostructures contained large number of defects and Ce<sup>3+</sup>. These defects might lead to the formation of a surface state energy band of oxygen. The oxygen adsorption, desorption and diffusion processes may occur easily on the surface of the 30 kGy-CeO<sub>2</sub> and 90 kGy-CeO<sub>2</sub>

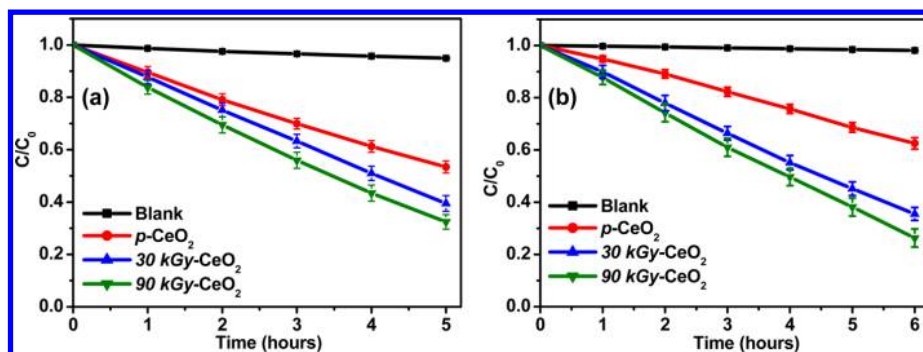


**Figure 7.** Photocatalytic degradation of (a) 4-NP and (b) MB by the visible light only (blank, i.e., without catalyst), p-CeO<sub>2</sub>, 30 kGy-CeO<sub>2</sub>, and 90 kGy-CeO<sub>2</sub> nanostructures.

nanostructures, that can greatly enhance their optical properties and imparts visible light photocatalytic activity.<sup>6,23</sup>

**Photocatalytic Degradation of 4-NP and MB by the p-CeO<sub>2</sub>, 30 kGy-CeO<sub>2</sub>, and 90 kGy-CeO<sub>2</sub> Nanostructures.** 4-NP is an important reagent used in the drugs and chemical industries, whereas MB is a hetero polyaromatic model dye used in the textile industry. 4-NP is highly toxic, whereas MB is mildly toxic. The photocatalytic activities were examined as reported earlier for the p-CeO<sub>2</sub>, 30 kGy-CeO<sub>2</sub>, and 90 kGy-CeO<sub>2</sub> nanostructures in the degradation of 4-NP and MB under visible light ( $\lambda > 400$  nm) illumination.<sup>19,20</sup> Both the 30 kGy-CeO<sub>2</sub> and 90 kGy-CeO<sub>2</sub> nanostructures showed better degradation than p-CeO<sub>2</sub>. The degradation was estimated from the decrease in the absorption intensity of 4-NP and MB at a fixed wavelength,  $\lambda_{\max} = 400$  and 665 nm respectively, during the course of the visible light photocatalytic degradation reaction. The degradation was calculated using  $C/C_0$ , where  $C_0$  is the initial concentration and  $C$  is the concentration after photoirradiation (Figure 7).<sup>34</sup> The blank experiment (Figure 7) did not show any degradation under visible light irradiation for 4-NP and MB. 90 kGy-CeO<sub>2</sub> showed better catalytic activity than 30 kGy-CeO<sub>2</sub>. The probable reasons for the enhanced photocatalytic activities compared to p-CeO<sub>2</sub> are the surface modification and defects in the 30 kGy-CeO<sub>2</sub> and 90 kGy-CeO<sub>2</sub> nanostructures. Oxygen vacancies, other defects and Ce<sup>3+</sup> centers enhance the photocatalytic activities and can be responsible for enhanced visible light photocatalytic activity.<sup>21,35</sup>

The BET measurements further support the highest photocatalytic performance of 90 kGy-CeO<sub>2</sub> (49.63 m<sup>2</sup>/g) as compared to 30 kGy-CeO<sub>2</sub> (42.04 m<sup>2</sup>/g) and p-CeO<sub>2</sub> (40.84 m<sup>2</sup>/g). The reason for the variation in the photocatalytic activities of the 30 kGy-CeO<sub>2</sub> and 90 kGy-CeO<sub>2</sub> nanostructures is also supported by DRS (Figure 2a) and PL (Figure 2b). These results suggest that the visible light photocatalytic activities of the 30 kGy-CeO<sub>2</sub> and 90 kGy-CeO<sub>2</sub> nanostructures were improved greatly by narrowing the band gap. Similarly, an EB dose-assisted increase in the photocatalytic activities was also observed for TiO<sub>2</sub>.<sup>19,21</sup>

From the above studies, discussion and proposed photo-decomposition mechanism (Figure 8), it is obvious that an EB is an effective tool for narrowing the band gap energy of semiconductor metal oxides, making it photoactive for the decomposition of toxic chemicals under visible light irradiation. Band gap excitation of the semiconductor results in electron-hole separation. The high oxidative potential of the hole in the photocatalyst allows the formation of reactive intermediates. Very reactive hydroxyl radicals ( $\cdot\text{OH}$ ) can also be formed,

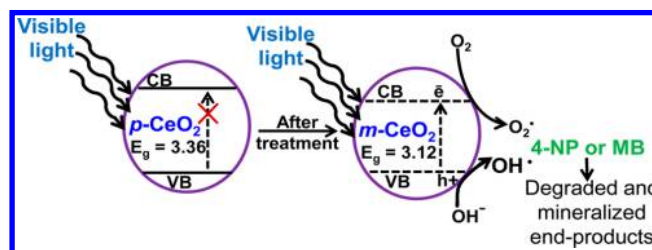


**Figure 8.** Proposed mechanism for the photodegradation of 4-NP and MB by the 90 kGy-CeO<sub>2</sub> nanostructures under visible light irradiation.

either by the decomposition of water or by the reaction of a hole with OH<sup>-</sup>.<sup>10,36,37</sup> The hydroxyl radicals and photo-generated holes are extremely strong, nonselective oxidants that lead to the degradation of 4-NP and MB at the surface of the 30 kGy-CeO<sub>2</sub> and 90 kGy-CeO<sub>2</sub> nanostructures. This can be attributed to the high concentrations of oxygen vacancies and defects created in the 30 kGy-CeO<sub>2</sub> and 90 kGy-CeO<sub>2</sub> nanostructures because the photocatalytic activity of 30 kGy-CeO<sub>2</sub> and 90 kGy-CeO<sub>2</sub> nanostructures is due to the high concentration of surface donor defects, such as oxygen vacancies and Ce<sup>3+</sup> centers.<sup>21,23,35</sup> When commercially available CeO<sub>2</sub> (Sigma) was irradiated with EB, 90 kGy EB irradiation produced more defects or surface modification in CeO<sub>2</sub> than 30 kGy EB irradiation to make CeO<sub>2</sub> photoactive in visible light. 90 kGy-CeO<sub>2</sub> showed higher photocatalytic activity than 30 kGy-CeO<sub>2</sub>, even though the difference in band gap was not significant. The increase in the photocatalytic activities might be due to surface a modification and oxygen vacancy which minimizes the recombination of photogenerated electrons and holes. Photocatalytic activity is supported by DRS, PL, and XPS.

**Stability and Reusability of the 90 kGy-CeO<sub>2</sub> Nanostructure.** The stability and reusability of the 90 kGy-CeO<sub>2</sub> nanostructure was tested by centrifuging the catalyst from the dye solutions (4-NP and MB), washing with DI water and drying in an oven at 100 °C. The reused catalyst showed ~95% and ~90% response for the second and third runs, respectively, in each case to that of the fresh catalyst (Figure S3, Supporting Information), which highlights the stability and reusability of the 90 kGy-CeO<sub>2</sub> nanostructure.

**Photoelectrochemical Studies of the p-CeO<sub>2</sub>, 30 kGy-CeO<sub>2</sub>, and 90 kGy-CeO<sub>2</sub> for Photoelectrodes.** The photoelectrochemical activity of the nanomaterials is determined by both the light-harvesting capacity and the separation of electron-hole pairs.<sup>6</sup> Therefore, electrochemical impedance spectroscopy (EIS) and linear scan voltammetry (LSV) under

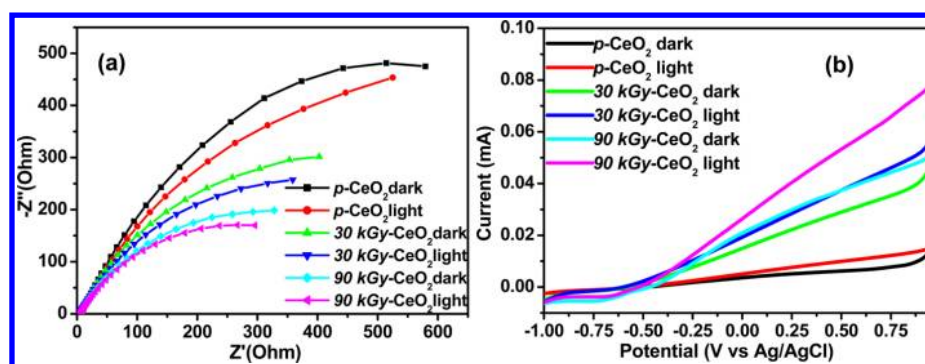


**Figure 9.** (a) Nyquist plots of the p-CeO<sub>2</sub>, 30 kGy-CeO<sub>2</sub> and 90 kGy-CeO<sub>2</sub> photocatalyst in the dark and under visible light irradiation, and (b) LSV curves for photocurrent response of the p-CeO<sub>2</sub>, 30 kGy-CeO<sub>2</sub> and 90 kGy-CeO<sub>2</sub> photoelectrodes in the dark and under visible light irradiation at a scan rate of 50 mV/s.

dark and visible light irradiation were performed to know the visible light activity and efficiency of charge separation of the 30 kGy-CeO<sub>2</sub> and 90 kGy-CeO<sub>2</sub> photoelectrodes.

**Electrochemical Impedance Spectroscopy.** EIS measurements were performed on p-CeO<sub>2</sub>, 30 kGy-CeO<sub>2</sub>, and 90 kGy-CeO<sub>2</sub> photocatalysts to examine the charge transfer resistance and separation efficiency between the photo-generated electrons and holes because the charge separation efficiency of photogenerated electrons and holes is a critical factor for the photocatalytic activity and photoelectrodes.<sup>38–41</sup>

Figure 9a shows the typical EIS Nyquist plots of the p-CeO<sub>2</sub>, 30 kGy-CeO<sub>2</sub>, and 90 kGy-CeO<sub>2</sub> photocatalysts in the dark and under visible light irradiation.<sup>40–42</sup> The arc radius of the EIS spectra reflects the interface layer resistance arising at the surface of the electrode.<sup>40</sup> A smaller arc radius indicates higher charge transfer efficiency.<sup>19,39,43</sup> The arc radii of the 30 kGy-CeO<sub>2</sub> and 90 kGy-CeO<sub>2</sub> photocatalysts were smaller than that of p-CeO<sub>2</sub> in the cases of dark and visible light irradiation. This suggests that the 30 kGy-CeO<sub>2</sub> and 90 kGy-CeO<sub>2</sub> photocatalysts has lower resistance than p-CeO<sub>2</sub>, which can accelerate the interfacial charge-transfer process. The arc radius of the 90 kGy-CeO<sub>2</sub> photocatalyst was smaller than that of the 30 kGy-CeO<sub>2</sub> in dark and under visible light irradiation. This suggests that the 90 kGy-CeO<sub>2</sub> photocatalyst has the lowest charge transfer resistance and is most suitable for photocatalytic applications. These observations are supported by the PL results and the visible light photocatalytic degradation of 4-NP and MB. The EIS results further support the important role of Ce<sup>3+</sup> and different types of defects and oxygen vacancies, which facilitate the charge separation (electrons and holes) and transfer efficiency of photogenerated electrons and holes on the surface of the 30 kGy-CeO<sub>2</sub> and 90 kGy-CeO<sub>2</sub> photocatalysts.<sup>39,40</sup>

**Linear Scan Voltammetry.** To investigate the possible mechanisms for the enhanced visible light photoactivity (i.e., photocurrent), LSV for p-CeO<sub>2</sub>, 30 kGy-CeO<sub>2</sub>, and 90 kGy-CeO<sub>2</sub> nanostructures were performed under the dark and visible light irradiation.<sup>19,40,42</sup> Figure 9b shows the improvement in the photocurrent response of 30 kGy-CeO<sub>2</sub> and 90 kGy-CeO<sub>2</sub> nanostructures which is attributed to the increase of light harvesting ability due to defects which gives narrowed band gap to 30 kGy- and 90 kGy-CeO<sub>2</sub>. Due to the narrow band gap the valence electrons can be excited to the conduction band by absorbing visible light. It is known that the photoelectrochemical activity is determined by both the capacity of light-harvesting and the separation of electron–

hole pairs. Therefore, electron–hole pairs are generated by absorbing the incident photons with energies larger than the  $E_g$  and they will recombine unless they are separated quickly.<sup>41–44</sup>

Generally, a high value of the photocurrent indicates that the sample holds strong ability to generate and transfer the photoexcited charge carrier under irradiation.<sup>40–47</sup> The 30 kGy-CeO<sub>2</sub> and 90 kGy-CeO<sub>2</sub> nanostructures show higher photocurrent than p-CeO<sub>2</sub> under the same condition, suggesting that the 30 kGy-CeO<sub>2</sub> and 90 kGy-CeO<sub>2</sub> nanostructures exhibits stronger ability in separation of electron–hole pairs than p-CeO<sub>2</sub>, as proven by the PL. However, the 90 kGy-CeO<sub>2</sub> nanostructures shows higher photocurrent than the 30 kGy-CeO<sub>2</sub> nanostructures. The significant improvement in the photocurrent for 90 kGy-CeO<sub>2</sub> nanostructures shows that it can be easily motivated by visible light, and produce more photoinduced carriers, thus possessing high visible photocatalytic activity. The EIS and LSV results show that the 90 kGy-CeO<sub>2</sub> nanostructures can be used effectively as photocatalysts and photoelectrode materials.

The difference in the appearance (Figure 2a) of the p-CeO<sub>2</sub> (white), 30 kGy-CeO<sub>2</sub> (light yellow), and 90 kGy-CeO<sub>2</sub> (pale yellow) photocatalysts suggests that there is a change in either the quantum state or energy absorbed by the nanostructures. DRS (Figure 2a) revealed a change in the band gap energy because the state change is quite difficult in CeO<sub>2</sub> without additional impurities, whereas energy absorption by the 30 kGy-CeO<sub>2</sub> and 90 kGy-CeO<sub>2</sub> nanostructures might be possible. A range of characterizations techniques, such as DRS, PL, XPS, Raman spectroscopy, and photoelectrochemical studies (EIS and LSV), highlighted the importance of Ce<sup>3+</sup> and different types of oxygen species in the 30 kGy-CeO<sub>2</sub> and 90 kGy-CeO<sub>2</sub> nanostructures relative to p-CeO<sub>2</sub> for visible light photocatalytic degradation reactions and photoelectrodes. The EB produces solvated electrons and other radicals, such as •OH, which might alter the ratio of Ce<sup>3+</sup>/Ce<sup>4+</sup> and oxygen species.<sup>19,21,23</sup> Moreover, Ce sites cannot be replaced because there is no other dopant in the system. Therefore, CeO<sub>2</sub> modification by an EB leads to either the addition of electrons or radicals to the CeO<sub>2</sub>, which makes the CeO<sub>2</sub> have different ratios of Ce<sup>3+</sup>/Ce<sup>4+</sup> and oxygen deficient/rich either by the addition of electrons or the replacement of oxygen from the CeO<sub>2</sub> matrix, in such a way that oxygen species residing at the surface of CeO<sub>2</sub> makes the matrix either oxygen deficient or rich.

## CONCLUSION

EB irradiation of two different doses (30 kGy and 90 kGy) was used for defect-induced band gap narrowing of CeO<sub>2</sub> for visible light photocatalytic activities and photoelectrodes. Defect induced band gap narrowing of CeO<sub>2</sub> nanostructure was confirmed by DRS, PL, XRD, Raman, XPS, and TEM. The p-CeO<sub>2</sub>, 30 kGy-CeO<sub>2</sub>, and 90 kGy-CeO<sub>2</sub> nanostructures were used to photodecompose 4-NP and MB. The 30 kGy-CeO<sub>2</sub> and 90 kGy-CeO<sub>2</sub> nanostructures showed much higher photocatalytic activity than p-CeO<sub>2</sub>. EIS confirmed the defect-induced band gap narrowing of CeO<sub>2</sub> by showing higher electron transfer and minimizing the recombination of photogenerated electrons and holes for the 30 kGy-CeO<sub>2</sub> and 90 kGy-CeO<sub>2</sub> nanostructures under visible light irradiation. LSV further confirms the enhanced visible light activity of the 30 kGy-CeO<sub>2</sub> and 90 kGy-CeO<sub>2</sub> nanostructures. This shows that EB can be used as an effective tool to reduce the band gap of metal oxides (semiconductors) for the enhanced visible light photocatalytic activities and photoelectrodes.

## ASSOCIATED CONTENT

### Supporting Information

Further additional information about UV-vis and XPS survey and C 1s spectra of CeO<sub>2</sub> nanostructures modified by Electron beam. C/C<sub>0</sub> plots of 4-NP and MB photodegradation by 90 kGy CeO<sub>2</sub>. This material is available free of charge via the Internet at <http://pubs.acs.org>.

## AUTHOR INFORMATION

### Corresponding Author

\*Tel: +82 53 810 2517. Fax: +82 53 810 4631. E-mail: mhcho@ynu.ac.kr.

### Notes

The authors declare no competing financial interest.

## ACKNOWLEDGMENTS

This study was supported by Basic Science Research Program through the National Research Foundation of Korea (NRF) funded by the Ministry of Education, Science and Technology (Grant No: 2012R1A1A4A01005951).

## REFERENCES

- (1) Campbell, C. T.; Peden, C. H. F. Oxygen Vacancies and Catalysis on Ceria Surfaces. *Science* **2005**, *309*, 713–714.
- (2) Chueh, W. C.; Falter, C.; Abbott, M.; Scipio, D.; Furler, P.; Haile, S. M.; Steinfeld, A. High-flux Solar-driven Thermochemical Dissociation of CO<sub>2</sub> and H<sub>2</sub>O using Nonstoichiometric Ceria. *Science* **2010**, *330*, 1797–1800.
- (3) Esch, F.; Fabris, S.; Zhou, L.; Montini, T.; Africh, C.; Fornasiero, P.; Comelli, G.; Rosei, R. Electron Localization Determines Defect Formation on Ceria Substrates. *Science* **2005**, *309*, 752–755.
- (4) Chen, J.; Patil, S.; Seal, S.; McGinnis, J. F. Rare Earth Nanoparticles Prevent Retinal Degeneration Induced by Intracellular Peroxides. *Nat. Nanotechnol.* **2006**, *1*, 142–150.
- (5) Amin, K. A.; Hassan, M. S.; Awad, E. T.; Hashem, K. S. The Protective Effects of Cerium Oxide Nanoparticles against Hepatic Oxidative Damage Induced by Monocrotaline. *Inter. J. Nanomed.* **2011**, *6*, 143–149.
- (6) Lu, X.; Zheng, D.; Zhang, P.; Liang, C.; Liu, P.; Tong, Y. Facile Synthesis of Free-standing CeO<sub>2</sub> Nanorods for Photoelectrochemical Applications. *Chem. Commun.* **2010**, *46*, 7721–7723.
- (7) Mao, C.; Zhao, Y.; Qiu, X.; Zhu, J.; Burda, C. Synthesis, Characterization and Computational Study of Nitrogen-doped CeO<sub>2</sub>

Nanoparticles with Visible-light Activity. *Phys. Chem. Chem. Phys.* **2008**, *10*, 5633–5638.

- (8) Zhang, N.; Fu, X.; Xu, Y. J. A Facile and Green Approach to Synthesize Pt@CeO<sub>2</sub> Nanocomposite with Tunable Core-Shell and Yolk-Shell Structure and its Application as a Visible Light Photocatalyst. *J. Mater. Chem.* **2011**, *21*, 8152–8158.

- (9) Khan, M. M.; Kalathil, S.; Lee, J.; Cho, M. H. Enhancement in the Photocatalytic Activity of Au@TiO<sub>2</sub> Nanocomposites by Pretreatment of TiO<sub>2</sub> with UV Light. *Bull. Korean Chem. Soc.* **2012**, *33*, 1753–1758.

- (10) Khan, M. M.; Ansari, S. A.; Amal, M. I.; Lee, J.; Cho, M. H. Highly Visible Light Active Ag@TiO<sub>2</sub> Nanocomposites Synthesized Using an Electrochemically Active Biofilm: A Novel Biogenic Approach. *Nanoscale* **2013**, *5*, 4427–4435.

- (11) Inoue, T.; Nakata, Y.; Shida, S. Electron Beam Induced Orientation Selective Epitaxial Growth of CeO<sub>2</sub>(100) Layers on Si(100) Substrates by DC Reactive Sputtering. *J. Phys.: Conf. Ser.* **2008**, *100*, 082014(1–4).

- (12) Porqueras, I.; Person, C.; Corbella, C.; Vives, M.; Pinyol, A.; Bertran, E. Characteristics of E-beam Deposited Electrochromic CeO<sub>2</sub> Thin Films. *Solid State Ionics* **2003**, *165*, 131–137.

- (13) Zhang, Y.; Edmondson, P. D.; Varga, T.; Moll, S.; Namavar, F.; Lan, C.; Weber, W. J. Structural Modification of Nanocrystalline Ceria by Ion Beams. *Phys. Chem. Chem. Phys.* **2011**, *13*, 11946–11950.

- (14) Ramasamy, P.; Guha, S.; Shibu, E. S.; Sreeprasad, T. S.; Bag, S.; Banerjee, A.; Pradeep, T. Size Tuning of Au Nanoparticles formed by Electron Beam Irradiation of Au<sub>25</sub> Quantum Clusters Anchored within and Outside of Dipeptide Nanotubes. *J. Mater. Chem.* **2009**, *19*, 8456–8462.

- (15) Ami, T.; Ishida, Y.; Nagasawa, N.; Machida, A.; Suzuki, M. Room-temperature Epitaxial Growth of CeO<sub>2</sub>(001) Thin Films on Si(001) Substrates by Electron Beam Evaporation. *Appl. Phys. Lett.* **2001**, *78*, 1361–1363.

- (16) Tatar, B.; Sam, E. D.; Kutlu, K.; Urgen, M. Synthesis and Optical Properties of CeO<sub>2</sub> Nanocrystalline Films Grown by Pulsed Electron Beam Deposition. *J. Mater. Sci.* **2008**, *43*, 5102–5108.

- (17) Surmacki, J.; Wronski, P.; Szadkowska-Nicze, M.; Abramczyk, H. Raman Spectroscopy of Visible-light Photocatalyst–Nitrogen-doped Titanium Dioxide Generated by Irradiation with Electron Beam. *Chem. Phys. Lett.* **2013**, *566*, 54–59.

- (18) Bzdon, S.; Goralski, J.; Maniukiewicz, W.; Perkowski, J.; Rogowski, J.; Szadkowska-Nicze, M. Radiation-induced Synthesis of Fe-doped TiO<sub>2</sub>: Characterization and Catalytic Properties. *Radiat. Phys. Chem.* **2012**, *81*, 322–330.

- (19) Khan, M. M.; Ansari, S. A.; Pradhan, D.; Ansari, M. O.; Han, D. H.; Lee, J.; Cho, M. H. Band Gap Engineered TiO<sub>2</sub> Nanoparticles for Visible Light Induced Photoelectrochemical and Photocatalytic Studies. *J. Mater. Chem. A* **2014**, *2*, 637–644.

- (20) Kalathil, S.; Khan, M. M.; Ansari, S. A.; Lee, J.; Cho, M. H. Band Gap Narrowing of Titanium Dioxide (TiO<sub>2</sub>) Nanocrystals by Electrochemically Active Biofilms and their Visible Light Activity. *Nanoscale* **2013**, *5*, 6323–6326.

- (21) Kim, M. J.; Kim, K. D.; Tai, W. S.; Seo, H. O.; Luo, Y.; Kim, Y. D.; Lee, B. C.; Park, O. K. Enhancement of Photocatalytic Activity of TiO<sub>2</sub> by High-energy Electron-beam Treatment under Atmospheric Pressure. *Catal. Lett.* **2010**, *135*, 57–61.

- (22) Lin, H. L.; Wu, C. Y.; Chiang, R. K. Facile Synthesis of CeO<sub>2</sub> Nanoplates and Nanorods by [100] Oriented Growth. *J. Colloid Interface Sci.* **2010**, *341*, 12–17.

- (23) Choudhury, B.; Choudhury, A. Ce<sup>3+</sup> and Oxygen Vacancy Mediated Tuning of Structural and Optical Properties of CeO<sub>2</sub> Nanoparticles. *Mater. Chem. Phys.* **2012**, *131*, 666–671.

- (24) Patsalas, P.; Logothetidis, S. Structure-dependent Electronic Properties of Nanocrystalline Cerium Oxide Films. *Phys. Rev. B* **2003**, *68*, 035104 (1–13).

- (25) Liqiang, J.; Yichun, Q.; Baiqi, W.; Shudan, L.; Baojiang, J.; Libin, Y.; Wei, F.; Honggang, F.; Jiazhong, S. Review of Photoluminescence Performance of Nano-sized Semiconductor Materials and its Relationships with Photocatalytic Activity. *Sol. Energy Mater. Sol. Cells* **2006**, *90*, 1773–1787.

- (26) Ansari, S. A.; Khan, M. M.; Ansari, M. O.; Lee, J.; Cho, M. H. Band Gap Engineering of CeO<sub>2</sub> Nanostructure using an Electrochemically Active Biofilm for Visible Light Applications. *RSC Adv.* **2014**, *4*, 16782–16791.
- (27) Shehata, N.; Meehan, K.; Hudait, M.; Jain, N. Control of Oxygen Vacancies and Ce<sup>+3</sup> Concentrations in Doped Ceria Nanoparticles via the Selection of Lanthanide Element. *J. Nanopart. Res.* **2012**, *14*, 1173–1183.
- (28) Liqiang, J.; Xiaojun, S.; Baifu, X.; Baiqi, W.; Weimin, C.; Honggang, F. The Preparation and Characterization of La Doped TiO<sub>2</sub> Nanoparticles and their Photocatalytic Activity. *J. Solid State Chem.* **2004**, *177*, 3375–3382.
- (29) Zhang, F.; Chan, S.-W.; Spanier, J. E.; Apak, E.; Jin, Q.; Robinson, R. D.; Herman, I. P. Cerium Oxide Nanoparticles: Size-selective Formation and Structure Analysis. *Appl. Phys. Lett.* **2002**, *80*, 127–129.
- (30) Cullity, B. D.; Stock, S. R. Elements of X-ray Diffraction; Prentice Hall: Englewood Cliffs, NJ, 2001.
- (31) Spanier, J. E.; Robinson, R. D.; Zhang, F.; Chan, S. W.; Herman, I. P. Size-dependent Properties of CeO<sub>2,y</sub> Nanoparticles as Studied by Raman Scattering. *Phys. Rev. B* **2001**, *64*, 245407 (1–8).
- (32) Meng, F.; Wang, L.; Cui, J. Controllable Synthesis and Optical Properties of Nano-CeO<sub>2</sub> via a Facile Hydrothermal Route. *J. Alloys Compd.* **2013**, *556*, 102–108.
- (33) Li, H.; Wang, G.; Zhang, F.; Cai, Y.; Wang, Y.; Djerdj, I. Surfactant-assisted Synthesis of CeO<sub>2</sub> Nanoparticles and their Application in Wastewater Treatment. *RSC Adv.* **2012**, *2*, 12413–12423.
- (34) Zhang, N.; Zhang, Y.; Xu, Y. J. Recent Progress on Graphene-based Photocatalysts: Current Status and Future Perspectives. *Nanoscale* **2012**, *4*, 5792–5813.
- (35) Lu, X.; Zhai, T.; Cui, H.; Shi, J.; Xie, S.; Huang, Y.; Liang, C.; Tong, Y. Redox Cycles Promoting Photocatalytic Hydrogen Evolution of CeO<sub>2</sub> Nanorods. *J. Mater. Chem.* **2011**, *21*, 5569–5572.
- (36) Zhang, N.; Liu, S.; Xu, Y. J. Recent Progress on Metal Core@Semiconductor Shell Nanocomposites as a Promising Type of Photocatalyst. *Nanoscale* **2012**, *4*, 2227–2238.
- (37) Yang, M. Q.; Xu, Y. J. Selective Photoredox using Graphene-based Composite Photocatalysts. *Phys. Chem. Chem. Phys.* **2013**, *15*, 19102–19118.
- (38) Ansari, S. A.; Khan, M. M.; Lee, J.; Cho, M. H. Highly Visible Light Active Ag@ZnO Nanocomposites Synthesized by Gel-Combustion Route. *J. Ind. Eng. Chem.* **2014**, *20*, 1602–1607.
- (39) Leng, W. H.; Zhang, Z.; Zhang, J. Q.; Cao, C. N. Investigation of the Kinetics of a TiO<sub>2</sub> Photoelectrocatalytic Reaction Involving Charge Transfer and Recombination through Surface States by Electrochemical Impedance Spectroscopy. *J. Phys. Chem. B* **2005**, *109*, 15008–15023.
- (40) Bai, X.; Wang, L.; Zong, R.; Lv, Y.; Sun, Y.; Zhu, Y. Performance Enhancement of ZnO Photocatalyst via Synergic Effect of Surface Oxygen Defect and Graphene hybridization. *Langmuir* **2013**, *29*, 3097–3105.
- (41) Ansari, S. A.; Khan, M. M.; Kalathil, S.; Nisar, A.; Lee, J.; Cho, M. H. Oxygen Vacancy Induced Band Gap Narrowing of ZnO Nanostructures by an Electrochemically Active Biofilm. *Nanoscale* **2013**, *5*, 9238–9246.
- (42) Gan, J.; Lu, X.; Wu, J.; Xie, S.; Zhai, T.; Yu, M.; Zhang, Z.; Mao, Y.; Wang, S. C.; Shen, Y.; Tong, Y. Oxygen Vacancies Promoting Photoelectrochemical Performance of In<sub>2</sub>O<sub>3</sub> Nanocubes. *Sci. Rep.* **2013**, *3*, 1021–1028.
- (43) Zhang, N.; Xu, Y. J. Aggregation- and Leaching-Resistant, Reusable, and Multifunctional Pd@CeO<sub>2</sub> as a Robust Nanocatalyst Achieved by a Hollow Core–Shell Strategy. *Chem. Mater.* **2013**, *25*, 1979–1988.
- (44) Li, W.; Li, M.; Xie, S.; Zhai, T.; Yu, M.; Liang, C.; Ouyang, X.; Lu, X.; Li, H.; Tong, Y. Improving the Photoelectrochemical and Photocatalytic Performance of CdO Nanorods with CdS Decoration. *CrystEngComm* **2013**, *15*, 4212–4216.
- (45) Ansari, S. A.; Khan, M. M.; Ansari, M. O.; Lee, J.; Cho, M. H. Biogenic Synthesis, Photocatalytic and Photoelectrochemical Performance of Ag–ZnO Nanocomposite. *J. Phys. Chem. C* **2013**, *117*, 27023–27030.
- (46) Khan, M. M.; Ansari, S. A.; Ansari, M. O.; Min, B. K.; Lee, J.; Cho, M. H. Biogenic Fabrication of Au@CeO<sub>2</sub> Nanocomposite with Enhanced Visible Light Activity. *J. Phys. Chem. C* **2014**, *118*, 9477–9484.
- (47) Ansari, S. A.; Khan, M. M.; Ansari, M. O.; Lee, J.; Cho, M. H. Highly Photoactive SnO<sub>2</sub> Nanostructures Engineered by Electrochemically Active Biofilm. *New J. Chem.* **2014**, *38*, 2462–2469.